



Self-assembled hollow sphere shaped Bi_2WO_6 /RGO composites for efficient sunlight-driven photocatalytic degradation of organic pollutants



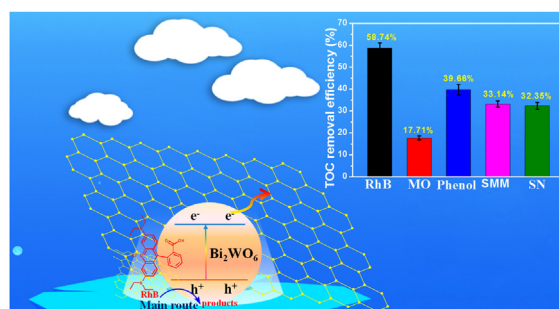
Shuying Dong, Xuhui Ding, Teng Guo, Xiaoping Yue, Xiao Han, Jianhui Sun*

School of Environment, Henan Normal University, Key Laboratory for Yellow River and Huai River Water Environmental and Pollution Control, Ministry of Education, Henan Key Laboratory for Environmental Pollution Control, Xinxiang, Henan 453007, PR China

HIGHLIGHTS

- Simple synthesis of hollow microsphere shaped Bi_2WO_6 /RGO hybrids was presented.
- Bi_2WO_6 /RGO enabled the effective degradation towards five pollutants under natural sunlight irradiation.
- Different mineralization of the five pollutants appeared in the presence of BWG-1.
- The origin of the enhanced photocatalytic performances of BWG-1 was discussed.
- Formation mechanism of Bi_2WO_6 /RGO composites was proposed.

GRAPHICAL ABSTRACT



ARTICLE INFO

Article history:

Received 15 October 2016
Received in revised form 25 January 2017
Accepted 4 February 2017
Available online 8 February 2017

Keywords:

Bi_2WO_6
Graphene
Natural sunlight
Photocatalytic
Wastewater

ABSTRACT

The urge to purify refractory organic wastewater without secondary pollution is pushing forward the use of photocatalysis. However, the complicated preparation procedures and low visible-light utilization efficiencies of currently-employed photocatalytic materials limit its practical applications. Herein, we design a facile and cost-effective route for the controllable synthesis of hollow sphere shaped Bi_2WO_6 /reduced graphene oxide (RGO) composites, which can efficiently degrade five organic wastewater, including rhodamine B, methyl orange, phenol, sulfamonomethoxine and sulfanilamide. The as-prepared Bi_2WO_6 /RGO hybrids were well characterized and exhibited much advanced sunlight-driven photocatalytic activity as compared to that of the pure Bi_2WO_6 . Such a high performance could be attributed to the enhanced light harvesting efficiency and improved charge separation efficiency in the composites. A possible formation mechanism of Bi_2WO_6 /RGO composite was also proposed. This study highlights the rational design of novel natural-sunlight-responsive photocatalyst.

© 2017 Elsevier B.V. All rights reserved.

1. Introduction

Currently, environmental problem with respect to organic wastewaters poses serious threats to both human health and

ecosystems. Conventional methodologies have not been able to effectively degrade such pollutants due to the fact that their detailed structures usually contain stable aromatic rings [1,2]. To this end, semiconductor photocatalysis offers a “green” and energy-saving technology for environmental remediation and converting photon energy into chemical energy [3]. It shows an extraordinary potential to decompose the toxic or harmful pollu-

* Corresponding author.

E-mail address: sunjhhj@163.com (J. Sun).

tants into harmless substances directly from the contaminant source under light irradiation [4,5]. However, photocatalysis has its certain drawbacks at the current stage, for instance, the photocatalytic activity could be limited due to the low quantum efficiency, poor visible light utilization efficiency, poor photostability and so on. In order to realize the practical use of photocatalysis, it is highly desirable to develop visible-light-responsive photocatalysts with augmented photocatalytic performances.

In recent years, Bi_2WO_6 has been proved to possess advanced photocatalytic activity for wastewater treatments under visible light irradiation [6]. As a promising photocatalyst, it possesses a plethora of advantages such as non-toxicity, high stability, low-cost, and relatively narrower band gap [7,8]. However, the photocatalytic activity of pure Bi_2WO_6 could be impeded by its rapid recombination of photogenerated carriers. Therefore, the modification of Bi_2WO_6 has by far received considerable attention, where various routes, e.g. substitution [9], heterostructure assembly [10,11], ions doping [12], noble-metal deposition [13] and carrier coupling [14], have been developed to improve the photocatalytic performance of pure Bi_2WO_6 .

Graphene, a two dimensional (2D) carbonaceous material with flexible layered feature, has boosted extensive research due to its chemical inertness, high specific surface area, excellent conductivity of charge carriers at room temperature and high thermal conductivity [15]. Moreover, the surface properties of graphene could be adjusted or tuned *via* appropriate modifications [16–18]. These unique physicochemical properties of graphene suggest that it can serve as an ideal platform material for hosting semiconductor photocatalysts. As such, graphene could reduce the recombination rate of photogenerated electron-hole pairs when coupling with semiconductors owing to the electron shuttle from the conjugated carbon network [19]. In addition, its theoretically large surface area can enhance adsorption activity and provide more active sites to anchor the pollutants, thereby increasing the photocatalytic performances [20–22]. Meanwhile, graphene-semiconductor hybrids would surprisingly show enhanced light absorption over almost the entire visible light wavelength region [23]. To date, graphene-based semiconductor composites have in general been synthesized using graphene oxide (GO) as the precursor, due to the fact that GO consists of graphite sheets covalently bonded with functional groups such as hydroxyl and epoxide groups on the basal planes and carboxyl groups at the edges [24]. This specific feature renders GO easily interact with cations and hence well accommodate the nucleation and growth of nanoparticles [25].

It is well realized that the photocatalytic activity is closely related with the micro-structure and macro-morphology of the photocatalyst [26]. The photocatalysts possessing hollow structures hold distinct advantages as compared to their solid counterparts. This could be attributed to the fact that the cavity structure may boost the effective use of light source *via* multiple reflections as well as enhance the transportation of reactants and products [27]. Templating method has been identified as a classic approach for synthesizing hollow structures, where the template cores can be removed by calcination or solvent extraction. However, this route is normally employed for the fabrication of simple metal oxide architectures because of the easy connection between the precursors and functional groups on the surface of the template. Multi-component oxide hollow structures are relatively difficult to obtain *via* such a templating method. Thus it is imperative to develop a proper way to prepare multi-component hollow oxides.

Herein, we report for the first time the tailored fabrication of Bi_2WO_6 /reduced graphene oxide (RGO) composites constructed by oriented nanosheets *via* a simple *in situ* hydrothermal method. The structures, morphologies, optical properties and photocatalytic properties were investigated in detail. The photocatalytic activities

of pure Bi_2WO_6 hollow spheres and Bi_2WO_6 /RGO composites were systematically evaluated by the photocatalytic degradation of five different types of model pollutants under natural sunlight irradiation, where the Bi_2WO_6 /RGO composites displayed enhanced sunlight-driven photocatalytic performances. Furthermore, the possible crystal growth mechanism for the formation of Bi_2WO_6 /RGO hybrid was tentatively proposed.

2. Experimental section

2.1. Synthesis of Bi_2WO_6 /RGO composite photocatalysts

GO was synthesized from natural graphite powders according to the recipe described in our previous study [28]. In a typical synthesis procedure, a specific amount of GO was well dispersed in 20 mL deionized water by high frequency ultrasonic treatment to get GO exfoliated, followed by adding 0.33 g $\text{Na}_2\text{WO}_4 \cdot 2\text{H}_2\text{O}$ into the solution to solution A. Meanwhile, 0.97 g $\text{Bi}(\text{NO}_3)_3 \cdot 5\text{H}_2\text{O}$ was dissolved in mixed solution of $\text{CH}_3\text{COOH}:\text{H}_2\text{O} = 1:4$ (v:v, 50 mL) to form solution B. Then A was added into B and transferred into a teflon-lined stainless steel autoclave and maintained at 180 °C for 3 h. The as-synthesized Bi_2WO_6 /RGO composites with 0, 0.25, 0.5, 1, 2, 3, 4, and 5 wt% RGO concentrations were labeled as BW, BWG-0.25, BWG-0.5, BWG-1, BWG-2, BWG-3, BWG-4, and BWG-5, respectively.

2.2. Characterizations

A Bruker-D8-AXS diffractometer system was used to record X-ray diffraction (XRD) patterns. The morphologies of obtained materials were inspected by using a JSM-6390LV scanning electron microscopy (SEM). Transmission electron microscopy (TEM) images and energy dispersive spectra (EDS) were collected on a Hitachi HT 7700 TEM system. Fourier transform infrared (FT-IR) spectra were performed on a FTIR Analyzer (Perkin-Elmer, Spectrum 400). X-ray photoelectron spectroscopy (XPS) measurements were carried out in an Escalab-250Xi X-ray photoelectron spectrometer microprobe. The nitrogen adsorption-desorption isotherms were investigated using a Micromeritics ASAP 2020 apparatus. The UV-Vis diffuse reflectance spectra (DRS) were obtained by using a UV-Vis-NIR spectrophotometer (Lambda 950, PerkinElmer). The photoluminescence (PL) spectra of photocatalysts were detected using a Fluorescence Spectrophotometer (FP-6500, Japan). The cyclic voltammetric (CV) and electrochemical impedance spectroscopy (EIS) were performed according to the recipe described in our previous study [29].

2.3. Evaluation of natural sunlight photocatalytic activity

The photocatalytic activities of Bi_2WO_6 and Bi_2WO_6 /RGO composites were monitored through the photodegradation of five different kinds of pollutants in aqueous solution under natural sunlight irradiation, including rhodamine B (RhB), methyl orange (MO), phenol, sulfamonomethoxine (SMM), and sulfanilamide (SN). All premeditated trials were performed between 8:30 a.m. and 4:30 p.m. on those sunny days to ensure the sufficient illumination of the natural sunlight. 200 mL aqueous solutions of RhB (60 $\text{mg}\cdot\text{L}^{-1}$), MO (10 $\text{mg}\cdot\text{L}^{-1}$), phenol (10 $\text{mg}\cdot\text{L}^{-1}$), SMM (10 $\text{mg}\cdot\text{L}^{-1}$), and SN (10 $\text{mg}\cdot\text{L}^{-1}$) were added to a batch of photochemical reactors. The concentrations of RhB, MO, phenol, SMM, and SN were analyzed using a UV-Vis spectrophotometer (UV-1700, SHIMADU) according to their absorbance at 553 nm, 463 nm, 270 nm, 273 nm, and 258 nm, respectively. The TOC of the samples were analyzed by using a TOC/TN Analyzer (VarioTOC, Elementar Analysensysteme GmbH, Germany).

3. Results and discussion

3.1. Probing the photocatalytic performances of $\text{Bi}_2\text{WO}_6/\text{RGO}$ composites

3.1.1. Effect of RGO dosages

Investigation of the photocatalytic activities of Bi_2WO_6 (BW) and $\text{Bi}_2\text{WO}_6/\text{RGO}$ composites with different RGO dosages were carried out throughout the degradation of $60 \text{ mg}\cdot\text{L}^{-1}$ RhB and $10 \text{ mg}\cdot\text{L}^{-1}$ MO under natural sunlight irradiation, as shown in Fig. 1a and b. Control blank study confirmed that neither RhB nor MO was prone to degradation by sunlight photolysis. Fig. 1a shows the comparison of the degradation of RhB in aqueous solution by BW and $\text{Bi}_2\text{WO}_6/\text{RGO}$ composites. Apparently, the introduction of RGO into the BW system promotes the degradation efficiency of RhB. Amongst them, BWG-1 and BWG-2 exhibit superior photocatalytic activity, indicating proper RGO content is crucial for augmenting the photocatalytic performances of the $\text{Bi}_2\text{WO}_6/\text{RGO}$ composites. Additionally, Fig. 1b shows the photocatalytic behaviors for the degradation of MO. The experimental results under the identical conditions clearly indicate that the photocatalytic activity order is consistent with the trend for the RhB degradation, where the BWG-1 and BWG-2 exhibit the enhanced photocatalytic activities. These results imply that the photocatalytic activity for degradation of RhB and MO on Bi_2WO_6 can be significantly improved via a suitable RGO dosage. In such cases, BWG-1 was used as the optimal photocatalyst for the following degradation reaction.

3.1.2. Effect of catalyst dosage and initial concentration of RhB

The effect of catalyst dosage on the degradation efficiency of fixed amount of RhB ($60 \text{ mg}\cdot\text{L}^{-1}$) was investigated, as shown in Fig. 1c. It is interesting to note that the degradation efficiency of RhB rises from 77% to 100% with increasing dosages of BWG-1 from 0.025 to 0.3 g. This phenomenon can be explained by the fact that the number of active photo-generated species accordingly increases with the increase of the catalyst dosage. However, further increasing the dosage of BWG-1 from 0.1 to 0.3 g is unreasonable due to cost concerns under such conditions. Therefore, in this regard, the optimal dosage of BWG-1 for the degradation of RhB is 0.1 g.

The influence of the initial concentration of RhB (ranging from 20 to $70 \text{ mg}\cdot\text{L}^{-1}$) on the photocatalytic degradation of RhB by fixed amount of BWG-1 (0.1 g) was tested, as shown in Fig. 1d. It is evident that RhB can be efficiently decolorized after 8 h photocatalytic reaction when the initial concentration was below $60 \text{ mg}\cdot\text{L}^{-1}$, while higher concentration ($70 \text{ mg}\cdot\text{L}^{-1}$) leads to the degradation efficiency slightly declining to 95%. This phenomenon might be attributed to the fact that higher concentration of RhB would sooner run out of as-generated radicals and decrease the sunlight utilization rate of BWG-1. Therefore, the proper concentration of RhB for this study was set at $60 \text{ mg}\cdot\text{L}^{-1}$.

3.1.3. Effect of pollutant species

With the consideration of practical usage of photocatalysts for real pollutant removal, the photocatalytic activity of the as-prepared $\text{Bi}_2\text{WO}_6/\text{RGO}$ composite (BWG-1) is further evaluated via the photocatalytic degradation of five model organic pollutants under sunlight irradiation. These include azo dye RhB and MO,

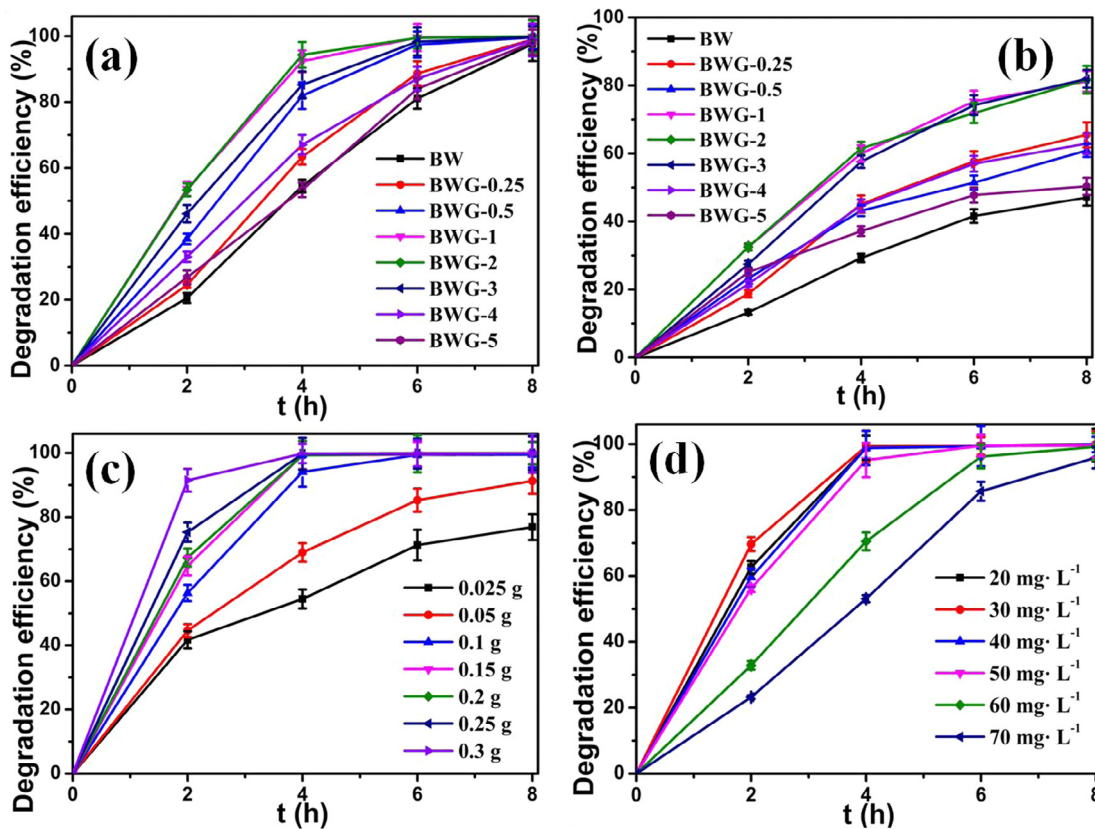


Fig. 1. The degradation efficiencies of the $60 \text{ mg}\cdot\text{L}^{-1}$ RhB (a) and $10 \text{ mg}\cdot\text{L}^{-1}$ MO (b) solution by hierarchical Bi_2WO_6 hollow microspheres (BW) and $\text{Bi}_2\text{WO}_6/\text{RGO}$ composites with different RGO dosages. ([catalyst] = 0.1 g). The degradation efficiencies of the RhB solution by (c) various BWG-1 dosage ([RhB] = $60 \text{ mg}\cdot\text{L}^{-1}$) and (d) various initial concentration of RhB ([BWG-1] = 0.1 g) under sunlight irradiation.

phenolic chemical phenol, antibiotic SMM and SN, the results of which are shown in Fig. 2. It can be seen that, in the absence of BWG-1, tiny amount of the model organic pollutants could be removed after 8 h sunlight irradiation. However, the five types of organic wastewater can be effectively degraded under sunlight irradiation with the addition of BWG-1, where the removal efficiency of RhB, MO, phenol, SMM and SN after 8 h reaction time reaches 99.5%, 78.5%, 66.5%, 70.9% and 57.6%, respectively. In order to further study the mineralization of the model organic pollutants by the prepared BWG-1 photocatalyst, the TOC removal efficiency of the wastewater was analyzed (Fig. 2b). The results reveal that the mineralization rate is commonly found to be in the order of $MO \ll SN < SMM < phenol < RhB$. Interestingly, the TOC removal efficiencies are lower than the degradation efficiencies, indicating that it is easier to destruct the chromophore of the organic pollutant rather than to mineralize them down to CO_2 and H_2O . Moreover, the as-fabricated BWG-1 displays different photocatalytic performances towards organic wastewater, which might be attributed to the fact that different organic molecules possess different adsorption characters as well as molecular architectures. To sum up, our Bi_2WO_6 /RGO composite is an efficient visible-light-response photocatalyst and might be potential for practical applications.

3.2. Detailed characterizations of the as-synthesized photocatalysts

XRD was employed to characterize the crystal phases of BW and Bi_2WO_6 /RGO composites. As shown in Fig. 3, all the samples present the typical XRD diffraction character of the orthorhombic Bi_2WO_6 phase (JCPDS 39-0256). However, no obvious diffraction peaks attributed to RGO can be detected in Bi_2WO_6 /RGO composites, which may be due to the fact that the low diffraction intensity, relatively small dosage amount and nice exfoliation of RGO in the composite, in good agreement with our previous study [30]. The results suggest that the incorporation of graphene in Bi_2WO_6 /RGO composites does not lead to the development of new crystal phase or changes in preferential orientations of Bi_2WO_6 .

The representative SEM images of BW and Bi_2WO_6 /RGO composites are shown in Fig. 4. Fig. 4a presents the top-view SEM observations of pure Bi_2WO_6 . It can be seen from the micrographs that the obtained Bi_2WO_6 are of monodisperse hierarchical microspheres with uniform size distributions. Each microsphere possesses a hollow structure and consists of numerous thin and curly nanosheets, as one is able to randomly observe the opening shells. By introducing graphene, the Bi_2WO_6 microspheres can still maintain their hierarchical morphology (Fig. 4b–g). Moreover, the stratiform RGO sheets are hardly observed due to the high and

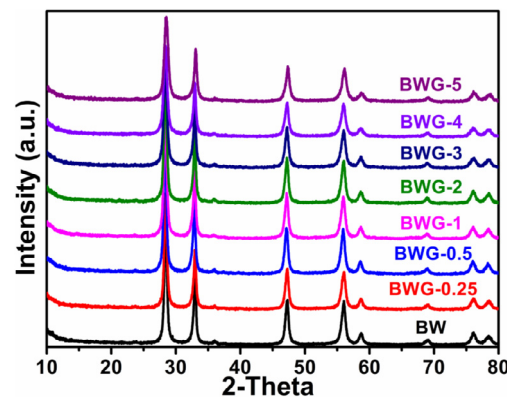


Fig. 3. XRD patterns of Bi_2WO_6 (BW) and Bi_2WO_6 /RGO composites with different RGO dosages.

uniform dispersion of RGO in Bi_2WO_6 /RGO composites. Further increasing the RGO dosage to 4 and 5% (wt) in the composites, the hierarchical Bi_2WO_6 hollow microspheres begin to deform (Fig. 4h and i), indicating that proper dosage of RGO plays an important role in maintaining the shape of Bi_2WO_6 photocatalysts.

TEM image of pure Bi_2WO_6 (Fig. 5a) and BWG-1 (Fig. 5b and c) further discloses the microsphere shape of an individual crystal. Fig. 5a shows that a pure Bi_2WO_6 is composed of sheets with different sizes, and the highlighted areas reveal that the microsphere possesses a hollow structure, in good agreement with the SEM observation. As for the composites, Fig. 5b clearly shows that the Bi_2WO_6 microsphere is coated with RGO nanosheets. Magnified image of the selected location in Fig. 5b is collected to show the RGO coating (Fig. 5c). Although the Bi_2WO_6 microspheres in BWG-1 could disassemble into thin sheets during the TEM sample preparation, the incorporated RGO seems not detached or damaged, suggesting the formation of stable Bi_2WO_6 /RGO hybrids. In addition, the EDS results show that the main elements of these samples were Bi, W and O. The errors of C content in the samples may be due to the small dosage and a relatively low atomic weight of RGO in the composites.

Fig. 6a shows FT-IR spectra of BW and BWG-1 products synthesized by hydrothermal reaction at 180 °C for 3 h, displaying several characteristic bands at 580, 733, 1385, 1628, and 3418 cm^{-1} . The BW and BWG-1 samples show main absorption bands at 400–1000 cm^{-1} , which are mainly attributed to Bi–O and W–O stretching [31]. Peaks at 733 cm^{-1} , 580 cm^{-1} and 1385 cm^{-1} are assigned to the stretching vibration modes of Bi–O, W–O, as well as W–O–W bridging stretching modes, respectively. The enhanced

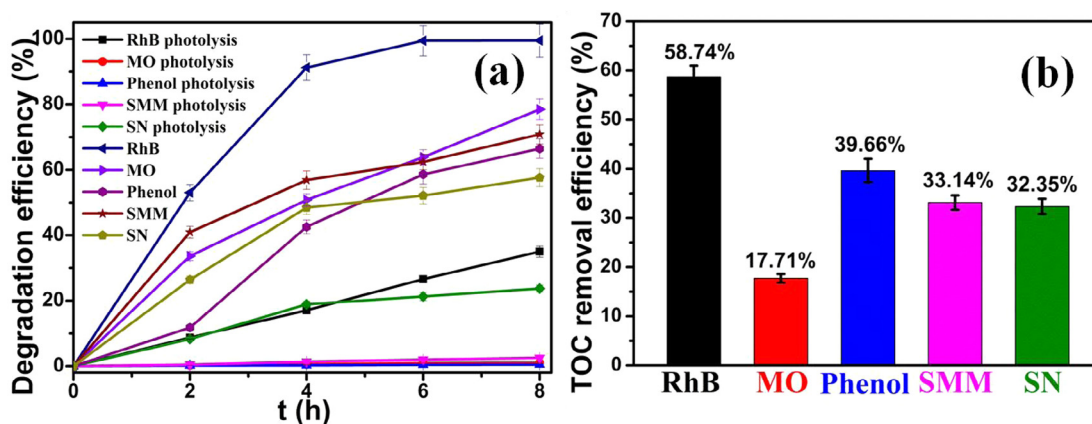


Fig. 2. Photocatalytic degradation efficiencies (a) and the corresponding TOC removal efficiencies (b) of RhB, MO, phenol, SMM and SN in the presence of BWG-1.

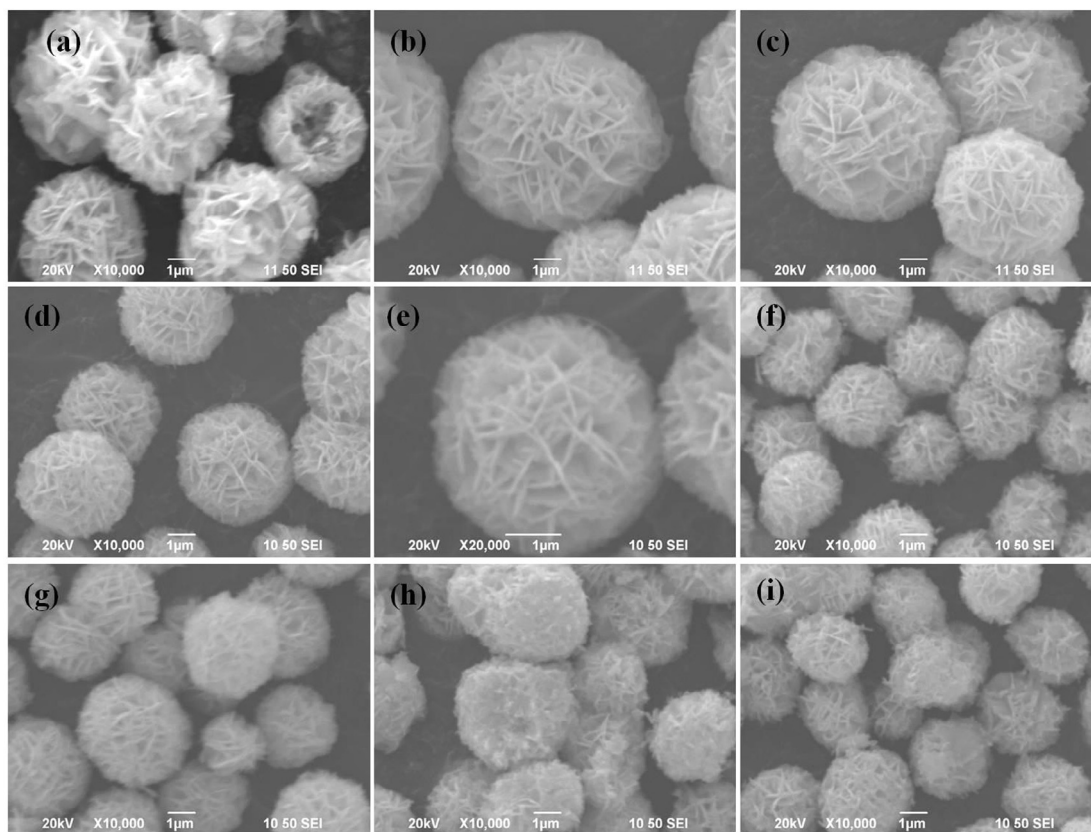


Fig. 4. SEM images of the prepared pure Bi_2WO_6 (a), BWG-0.25 (b), BWG-0.5 (c), BWG-1 (d, e), BWG-2 (f), BWG-3 (g), BWG-4 (h) and BWG-5 (i).

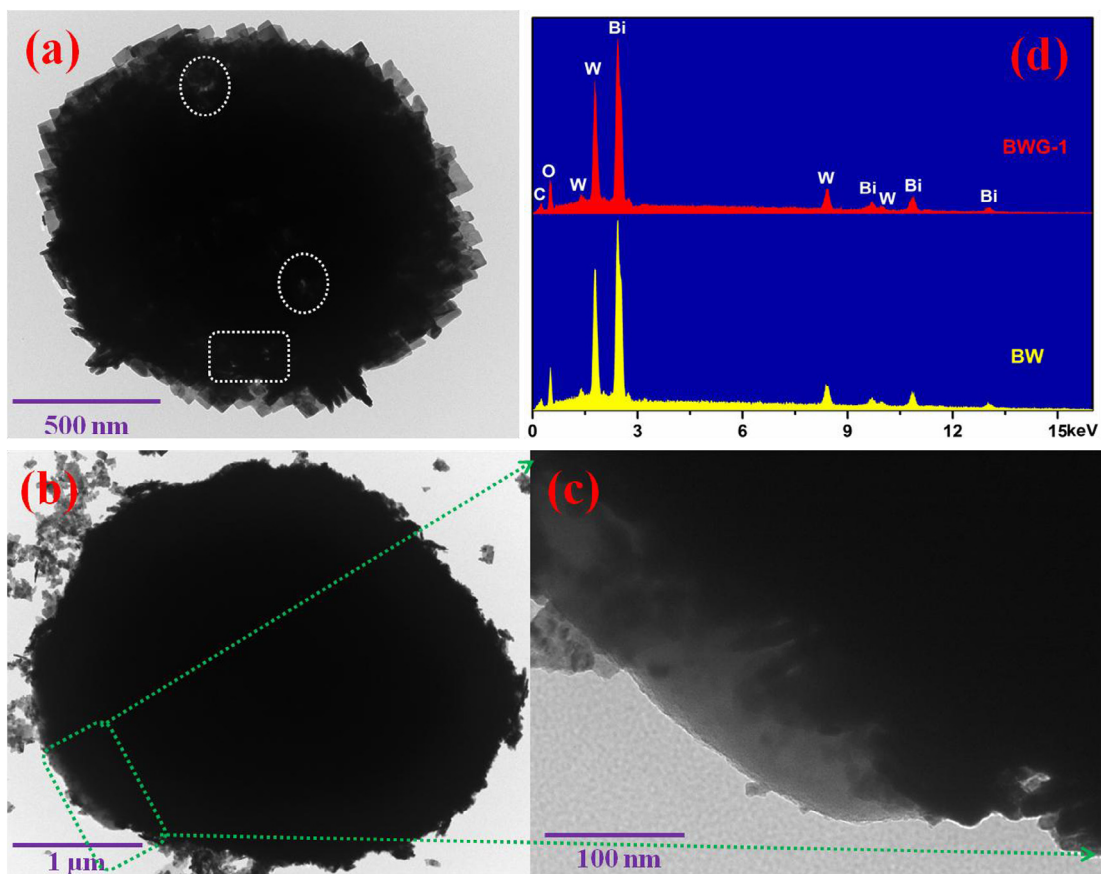


Fig. 5. TEM images and EDS (d) of pure Bi_2WO_6 (a) and BWG-1 (b and c).

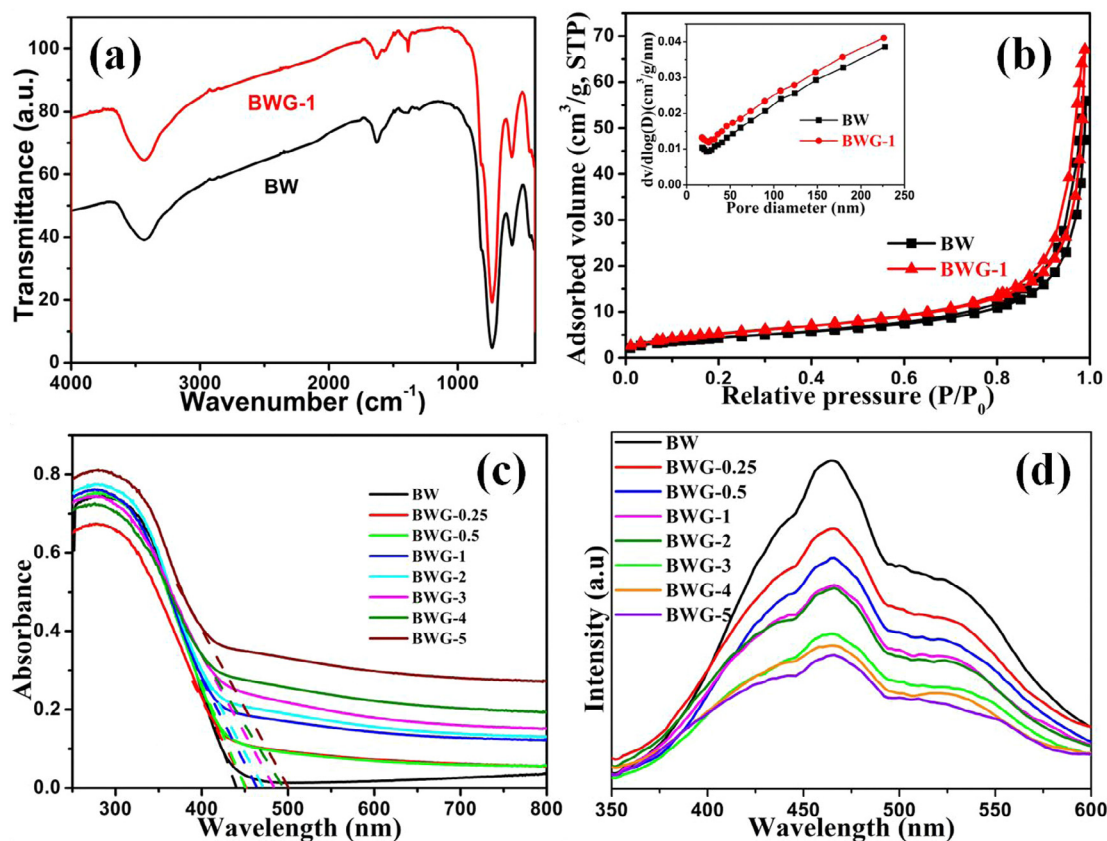


Fig. 6. (a) FT-IR spectra of the as-prepared BW and BWG-1. (b) Nitrogen adsorption-desorption isotherms of BW and BWG-1 with corresponding pore size distribution curves (inset). (c) UV-Vis DRS and (d) PL spectra of BW and Bi₂WO₆/RGO composites.

characteristic peak of 1385 cm⁻¹ in BWG-1 is attributed to the interface interaction between RGO and Bi₂WO₆ [32]. The peak at 1628 cm⁻¹ corresponds to the C=C stretching mode of graphene, while a broad band at 3418 cm⁻¹ is ascribed to O-H stretching vibrations of adsorbed water molecules on BW and BWG-1.

N₂ adsorption-desorption isotherms of BW and BWG-1 are collected to determine the surface area and pore diameter distribution, as shown in Fig. 6b. Both the BW and BWG-1 samples show similar adsorption-desorption features and pore diameter distributions (Fig. 6b inset). Both the isotherm curves for the BW and BWG-1 samples are of type IV, which is typically associated with capillary condensation in mesopores [33]. In the low relative pressure region ($P/P_0 < 0.6$), the adsorption and desorption curves coincide because they are monolayer adsorption and reversible. However, in the relatively high pressure region ($P/P_0 > 0.6$), both the isotherms have significant hysteresis, reflecting the formation of slit-shaped pores by the aggregation of Bi₂WO₆ nanosheets. The BET specific surface areas of BW and BWG-1 were calculated to be 16.1126 and 19.7927 m²·g⁻¹, respectively, suggesting that the introduction of RGO slightly increase the surface area of the final product. In addition, the corresponding pore size distribution curve of BW is consistent with that of BWG-1.

The light absorption property of the pure Bi₂WO₆ and Bi₂WO₆/RGO composites with different RGO dosage is analyzed *via* DRS, as shown in Fig. 6c. The absorption of pure Bi₂WO₆ lies from the UV to the visible light region (shorter than 450 nm), originating from the charge transfer response of Bi₂WO₆ from the valence band (VB) to the conduction band (CB). In terms of the Bi₂WO₆/RGO composites, the light harvesting capability within the visible light region enhanced with the increase of RGO dosages. In addition, an apparent red shift for Bi₂WO₆/RGO composites appears as compared to

pure Bi₂WO₆, which may be related to the charge-transfer transition between the CB or VB of RGO and BW [34]. These results suggest that the advanced photocatalytic activity of Bi₂WO₆/RGO composites might be partially attributed to the enhancement of light absorption.

It is well known that PL is a facile technique to study the photochemical properties of semiconductor materials, where the emission spectra are useful in determining the efficiency of charge carrier trapping, migration and transfer. A lower PL intensity might imply a lower recombination rate of the electron-hole pairs under light irradiation [35]. Fig. 6d shows the PL spectra of the prepared pure Bi₂WO₆ and Bi₂WO₆/RGO composites with different RGO dosages. When the excitation wavelength was set at 325 nm, all samples exhibit broad blue-green emission peaks at 430–550 nm. The strongest blue emission peak centered at ~465 nm is attributed to the intrinsic luminescence of Bi₂WO₆, originating from the photo-generated electron transfer transitions between the hybrid VB of Bi 6s and O 2p to the empty CB of W 5d orbital in WO₆²⁻ complex [36]. The weak green emission peak at 525 nm is ascribed to the defects of oxygen vacancies during the crystal growing process, which become the defect centers and thus affect the photochemical properties of Bi₂WO₆. Apparently, the PL intensities of Bi₂WO₆/RGO composites stay lower than that of pure Bi₂WO₆, indicating that the integration of RGO can efficiently suppress the recombination of photo-generated charge carriers.

The reduction degree of GO and the electronic interaction between BW and RGO in the composites were inspected by XPS. The survey XPS spectra of the BW and BWG-1 are shown in Fig. 7a, where the different binding energy are assigned to W 4f, Bi 4f, W 4d, C 1s, Bi 4d, O 1s and Bi 4p states. The C 1s peak in BW can be ascribed to residual traces from the precursor solution and/or the

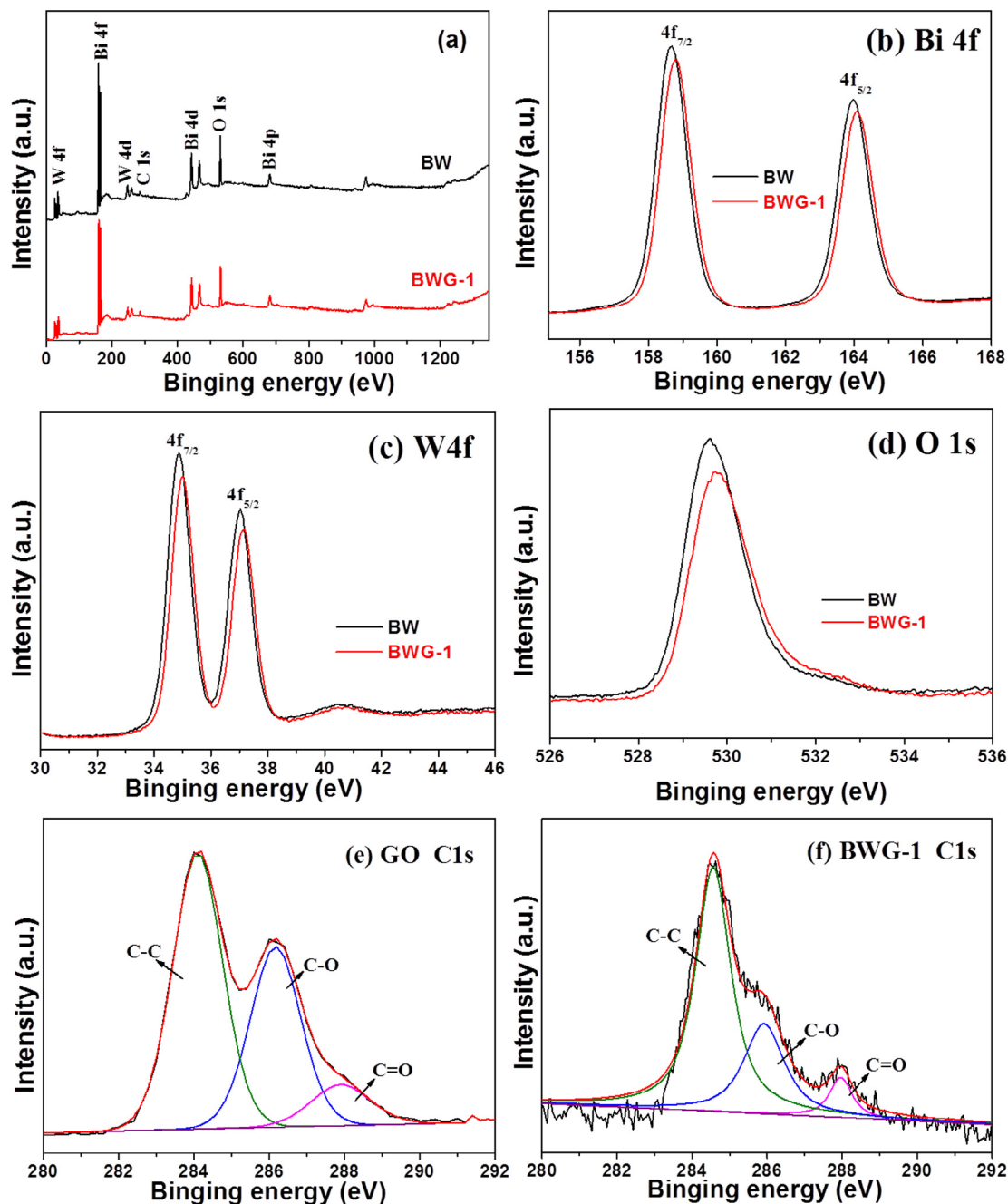


Fig. 7. XPS spectra of (a) BW and BWG-1, and high-resolution of (b) Bi 4f spectra, (c) W 4f spectra, (d) O 1s spectra; XPS spectra of C 1s in the (e) original GO and (f) BWG-1.

adventitious carbon from the XPS instrument itself. The high-resolution XPS spectra of the BW and BWG-1 were further collected. As shown in Fig. 7b–d, the peaks at 163.98 and 158.68 eV in BW correspond to Bi 4f 5/2 and Bi 4f 7/2, respectively, can be assigned to the Bi³⁺ oxidation state. The doublet peaks at 37.03 and 34.88 eV belong to W 4f 5/2 and W 4f 7/2, respectively, which are the features of W⁶⁺ oxidation state. In Fig. 7d, it is obvious that O 1s consists of one peak with the binding energy around 529.63 eV, which can be assigned to the O²⁻ reduction state. It is worth-noting that the characteristic peaks of Bi 4f, W 4f and O 1s over the BWG-1 composites shift toward higher binding energy by 0.1, 0.15 and 0.1 eV, respectively, suggesting a certain electronic interaction between Bi₂WO₆ and RGO in BWG-1 [34].

In addition, the C 1s XPS spectra of GO and BWG-1 are depicted in Fig. 7e and f. Three main peaks of C 1s from GO at 288.0, 286.2 and 284.2 eV are attributed to the C=O, C–O and C–C, respectively,

indicating a high percentage of oxygen-containing functional groups in GO (Fig. 7e). As for the BWG-1 composite, the peak intensities of the oxygenated functional groups display a dramatic decrease (Fig. 7f), which is in good agreement with the FT-IR results shown in Fig. 6a. This result indicates that most of the oxygen-containing functional groups were successfully removed, as GO was efficiently reduced to RGO after coupling with Bi₂WO₆ treated by our hydrothermal process. The reduction of GO would in turn enhance the electrical conductivity of the composites, and hence significantly improve the photocatalytic activity.

3.3. Possible mechanism of photocatalytic activity enhancement

The CV curves of BW and BWG-1 obtained at scan rate of 40 mV·S⁻¹ in a solution of 10 mM K₃Fe(CN)₆ and 0.1 M KCl are shown in Fig. 8a. Both the electrodes exhibit apparently reversible

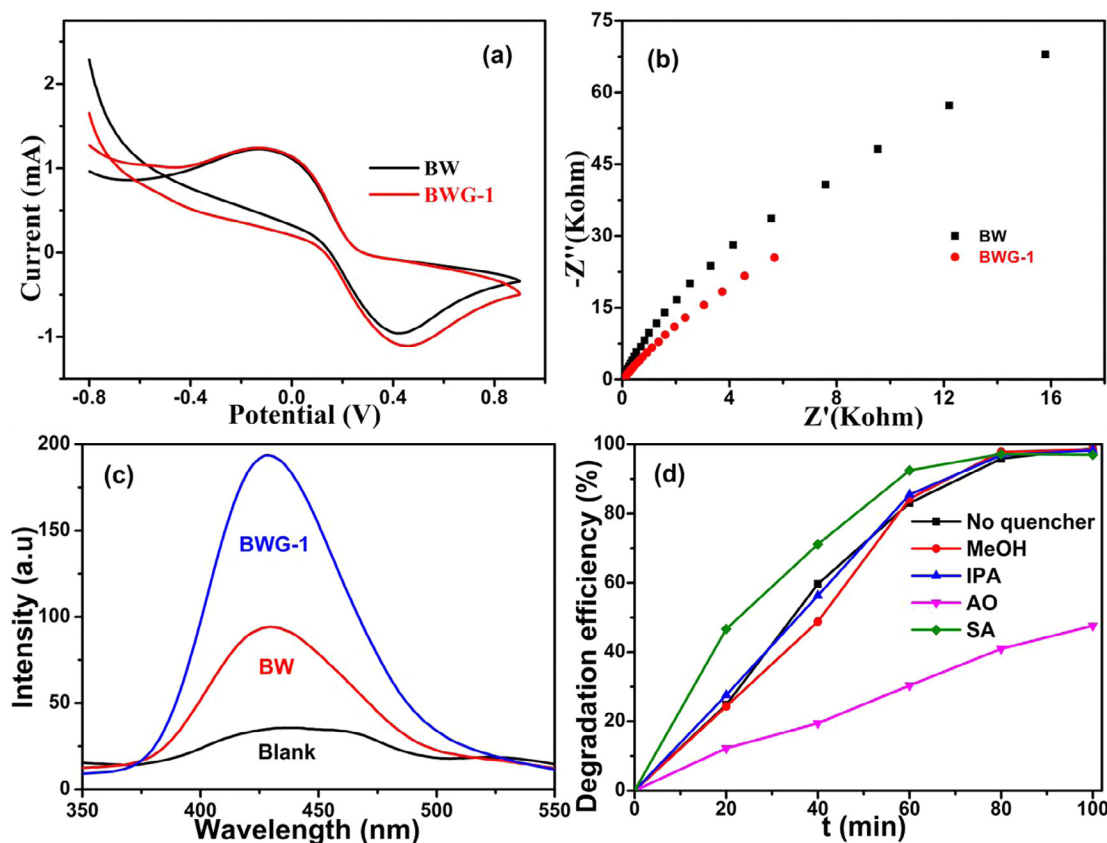


Fig. 8. (a) CV curves of the BW and BWG-1 electrodes in a solution of 10 mM $K_3Fe(CN)_6$ and 0.1 M KCl at scan rate of $40 \text{ mV}\cdot\text{s}^{-1}$ under visible light irradiation. (b) EIS curves of the BW and BWG-1 electrodes in a solution of 0.1 M Na_2SO_4 under visible light irradiation. (c) PL spectra of the BW and BWG-1 in TPA solution after visible light irradiation. (d) Trapping experiments of photocatalytic degradation of RhB over BWG-1 with/without the presence of scavengers.

voltammograms within potential windows ranging from -0.8 to 0.9 V, where the $Fe(CN)_6^{3-}/Fe(CN)_6^{4-}$ redox pairs are highly resolved at the BWG-1 electrode, resulting a higher redox current than that of the BW electrode. As depicted, the increased peak-to-peak separation and redox current show that the BWG-1 electrode fosters a faster electron transfer.

EIS is an informative technique to evaluate the charge transport in the electrochemical interfacial reactions. The EIS response of the BW and BWG-1 under visible light irradiation is shown in Fig. 8b. The reaction rate occurring at the surface of the electrode is proportional to the radius of the arc on the EIS Nyquist plot. Obviously, the radius for the BWG-1 (red curve) declines remarkably compared with that of the BW (black curve), indicating that both the charge-transfer resistance and solid state interface layer resistance have greatly decreased by the introduction of RGO. The faster interfacial charge transfer between the electron donor/acceptor within the BWG-1 benefits from the electron accepting and transporting properties of graphene, thereby giving rise to an effective separation of photo-generated electron-hole pairs. As a result, the photocatalytic oxidation rate is enhanced. In this regard, the results indicate that RGO can effectively suppress the charge recombination in the hybrid composites when served as an electron acceptor, thereby leading to a higher photocatalytic response.

Hydroxyl radical ($\cdot\text{OH}$) has been considered as an important reaction species in the photocatalytic degradation of many hazardous compounds due to its high reactivity to attack the organic structures [37–39]. $\cdot\text{OH}$ can be detected by using terephthalic acid (TPA) as a probe molecule, since TPA reacts readily with $\cdot\text{OH}$ to produce a highly fluorescent 2-hydroxyterephthalic acid, whose fluorescence intensity at 426 nm is in proportional to the amount of $\cdot\text{OH}$ produced in water. As shown in the PL spectra in Fig. 8c, both

the peak intensity of BW and BWG-1 was much higher than that of the blank test (no photocatalyst) under visible light irradiation, which elucidated that $\cdot\text{OH}$ on BW and BWG-1 catalyst was really produced under visible light irradiation. Additionally, the peak intensity of BWG-1 is greater than that of BW, suggesting the formation rate of $\cdot\text{OH}$ on the surface of BWG-1 is higher.

It is of paramount importance to evaluate the effect of the main active species during the photocatalytic reaction for elucidating the photocatalytic mechanism, where the detection can be realized through scavenging the relevant active species such as $\cdot\text{OH}$, h^+ , O_2^- and $^1\text{O}_2$ by using 1.0 mM isopropanol (IPA) ($\cdot\text{OH}$ scavenger), ammonium oxalate (AO) (h^+ scavenger), methyl alcohol (MeOH) (O_2^- scavenger) and sodium azide (SA) ($^1\text{O}_2$ scavenger), respectively [40–43]. Such a method is similar to the photocatalytic degradation test. As shown in Fig. 8d, the addition of IPA, MeOH or SA induces a small change in the photocatalytic degradation efficiencies of RhB. However, the photocatalytic activity of BWG-1 could be greatly suppressed by the addition of AO (an h^+ scavenger). Hence, the quenching effects of various scavengers suggest that the photogenerated holes are the dominant oxidative species for the degradation of RhB, where the $\cdot\text{OH}$ and O_2^- radicals play a minor role.

Based on the above experimental results, a possible photocatalytic degradation mechanism can be conjectured, as shown in Fig. 9. The reaction starts with the excitation of the BWG-1 photocatalyst by the sunlight irradiation, resulting in the generation and separation of holes (h^+) and electrons (e^-). Photoinduced e^- might react with O_2 to produce O_2^- radicals, while h^+ can directly oxidize the RhB adsorbed on the surface of BWG-1 into degradation products, which is regarded as the main degradation pathway in this reaction. Therefore, h^+ has few opportunities to react with OH^- /

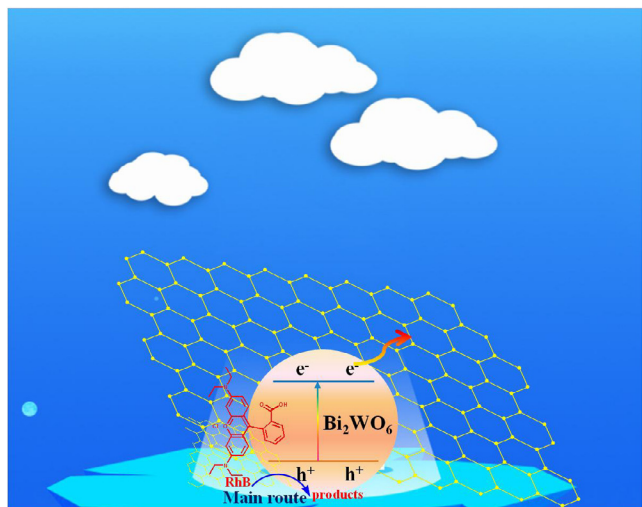


Fig. 9. Schematic illustration of the separation and transfer of photogenerated charges in the $\text{Bi}_2\text{WO}_6/\text{RGO}$ composites.

H_2O to form $\cdot\text{OH}$ radicals. Additionally, a conclusion could be drawn that the enhancement of the photocatalytic performance of BWG-1 should be ascribed to the increase of the light absorption intensity and range, as well as the effectively suppression of recombination of photon-generated carriers with the presence of RGO. However, the photocatalytic performance deteriorates when the RGO dosage is further increased above its optimal value.

Therefore, BWG-1 samples with 1 wt% RGO content possess the highest activity amongst all the prepared photocatalysts. The obtained results are similar with our previous report [29,30]. This phenomenon might be due to the fact that: (i) Such energy levels will be conducive to the photo-generated electrons in the CB of the BW transferring into the RGO, therefore leading to an effective charge separation; (ii) RGO may absorb some light and thus cause a light harvesting competition between BW and RGO with the increasing of RGO concentration, which result in poor photocatalytic performance; (iii) The excessive RGO can act as an electron-hole recombination center instead of providing an electron pathway and thus promote the recombination of charge carrier in RGO.

3.4. Discussing the formation of hierarchical $\text{Bi}_2\text{WO}_6/\text{RGO}$ hollow microspheres

To gain further understanding towards the shape formation mechanism of the $\text{Bi}_2\text{WO}_6/\text{RGO}$ hierarchical hollow microspheres, time-dependent investigations were carried out by extracting products at different reaction stages. Specifically, hydrothermal formation of BWG-1 was sampled at different reaction timeslots, namely, at 0 min (precursor), 40 min, 80 min, 100 min, 2 h, 3 h and 4 h. The SEM observations of the morphological evolution of the reaction products (Fig. 10a–f) suggest that the self-assembly growth process was dominated by Ostwald ripening mechanism. As shown in Fig. 10a, at the beginning, amorphous particles with random size distributions were formed by the direct mixing of the two solutions (A and B). Under hydrothermal treatment,

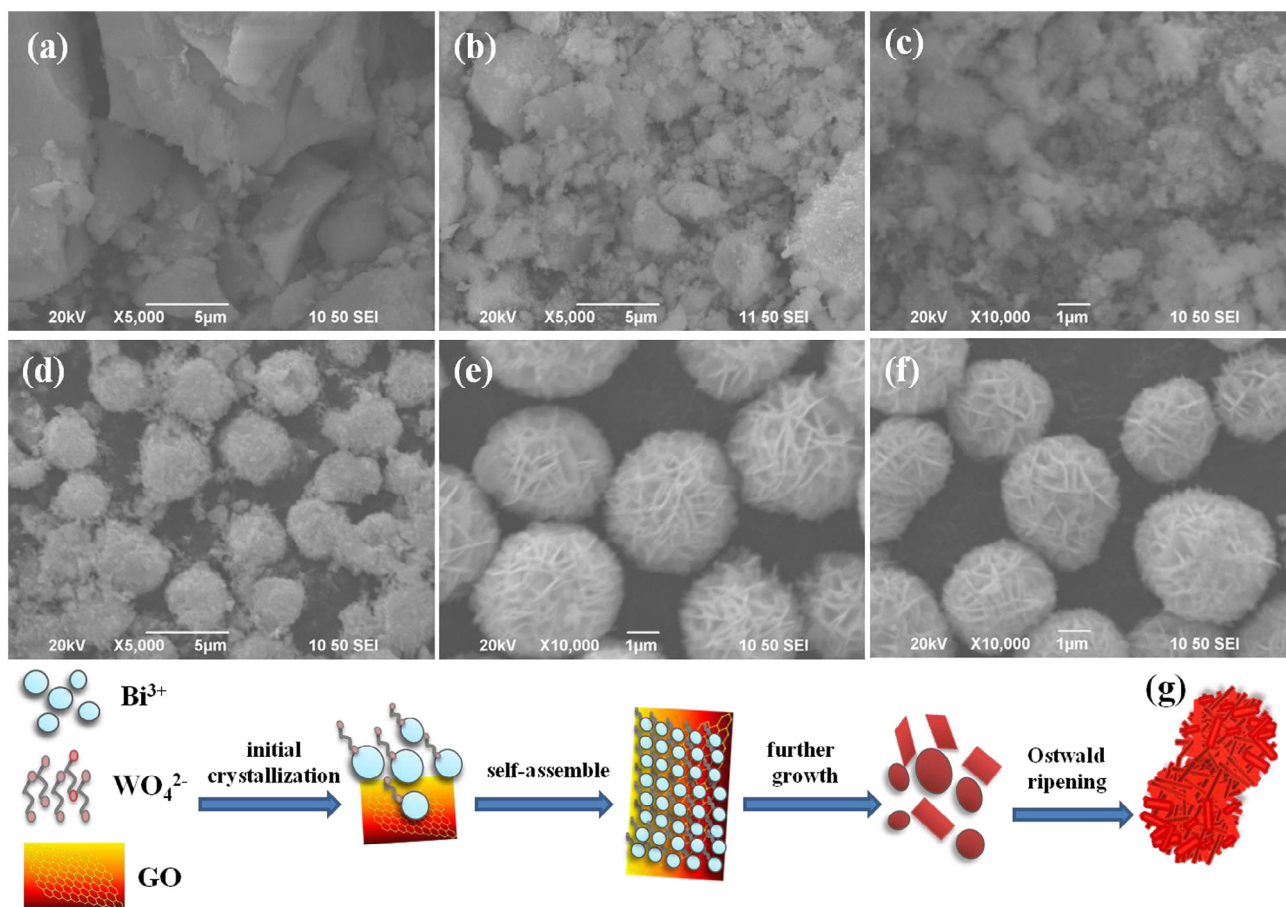


Fig. 10. SEM images depicting time-dependent morphological evolution of the $\text{Bi}_2\text{WO}_6/\text{RGO}$ composites (BWG-1) at different growth stages: (a) 0 min (precursor), (b) 40 min, (c) 100 min, (d) 2 h, (e) 3 h, and (f) 4 h; (g) The schematic diagram of crystal growth mechanism for the $\text{Bi}_2\text{WO}_6/\text{RGO}$ hierarchical microspheres.

BWG-1 crystal growth began from the formation of tiny crystalline nuclei in a supersaturated medium. In the earlier 100 min reaction (Fig. 10b and c), larger pieces eventually transformed to smaller particles, however, with increasing the reaction time to 2 h, the SEM image in Fig. 10d displays that the irregular BWG-1 nucleus generate via an “initial crystallization” process based on Gibbs-Thomson law. In this process, the intermediate samples show the coexistence of particles and irregular sphere structures (Fig. 10d). Further increasing the hydrothermal time to 3 h, the BWG-1 hierarchical sphere structure is more united due to Ostwald ripening, where the irregular particles vanished, indicating that the hollow spheres were grown at the cost of the smaller particles (Fig. 10e). No shape evolution of the BWG-1 samples occurred when the hydrothermal time was prolonged to 4 h (Fig. 10f). On the basis of the above analysis, a possible formation mechanism of the $\text{Bi}_2\text{WO}_6/\text{RGO}$ hierarchical microspheres was proposed, as shown in Fig. 10g.

Fig. 11a shows FT-IR spectra of BWG-1 samples collected at different hydrothermal reaction timeslots. The interactions between RGO and Bi_2WO_6 can be further confirmed by FT-IR analysis. It can be observed that the precursor exhibits absorptions at the same wavelength as those of synthesized samples, except at 1385 cm^{-1} . After hydrothermal treatment, new absorption peak at 1385 cm^{-1} can be attributed to the bridging stretching vibration of W-O-W, indicating the formation of Bi_2WO_6 molecules. Moreover, the broad IR bands at $400\text{--}1000\text{ cm}^{-1}$ gradually split into

specific single peaks with prolonging hydrothermal periods, which can be attributed to the stretching vibration of Bi-O and W-O. BWG-1 samples from the time-dependent investigation are further analyzed by XRD (Fig. 11b), the results of which are in good agreement with the SEM and FT-IR characterization. Prior to the hydrothermal reaction, the precursor displays no apparent peak; however, BWG-1 nanoparticles with low crystallinity are formed after 100 min hydrothermal reaction. When the reaction time reaches to 2 h, the orthorhombic Bi_2WO_6 phase quickly appears according to the XRD pattern of BWG-2 h. BWG-1 particles with high crystallinity are formed at 3 h hydrothermal treatment, after which the XRD patterns of the sampling remain unchanged with regard to the reaction time. Extending hydrothermal time to 4 h exerts no effect on the phase evolution of the BWG-1 samples.

3.5. Investigating the recycle performances of the representative BWG-1 photocatalyst

The durability of as-synthesized BWG-1 was evaluated by recycling the used catalyst. The degradation efficiency of RhB during each cycle (at the duration of 10 h) can reach 99%. The photocatalytic capacity of BWG-1 has not exhibited any significant loss even after five cycling runs (Fig. 12a). The BWG-1 composites employed in the recycle tests were also examined using XRD after the recycle experiments. The corresponding XRD pattern (Fig. 12b) reveals that there is no detectable difference between the

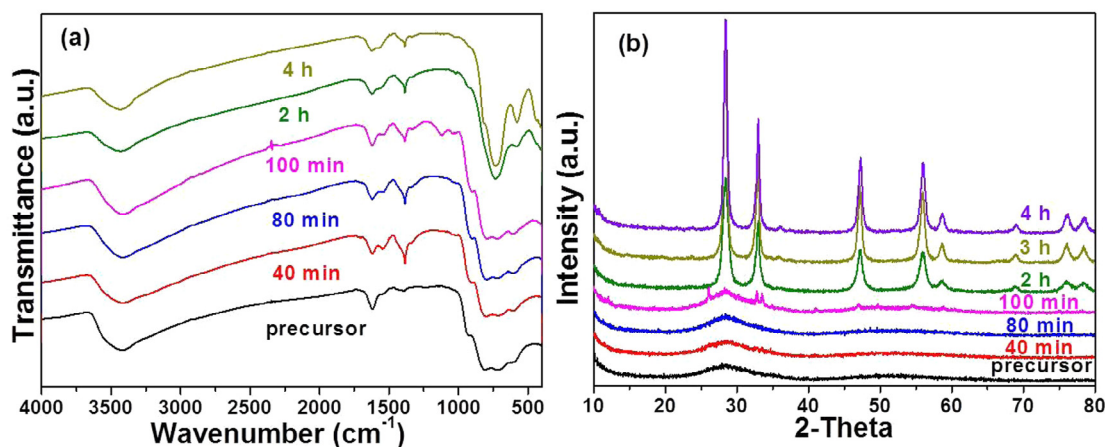


Fig. 11. (a) XRD patterns of the crystalline structure evolution and (b) FT-IR spectra of BWG-1 samples collected at different reaction times.

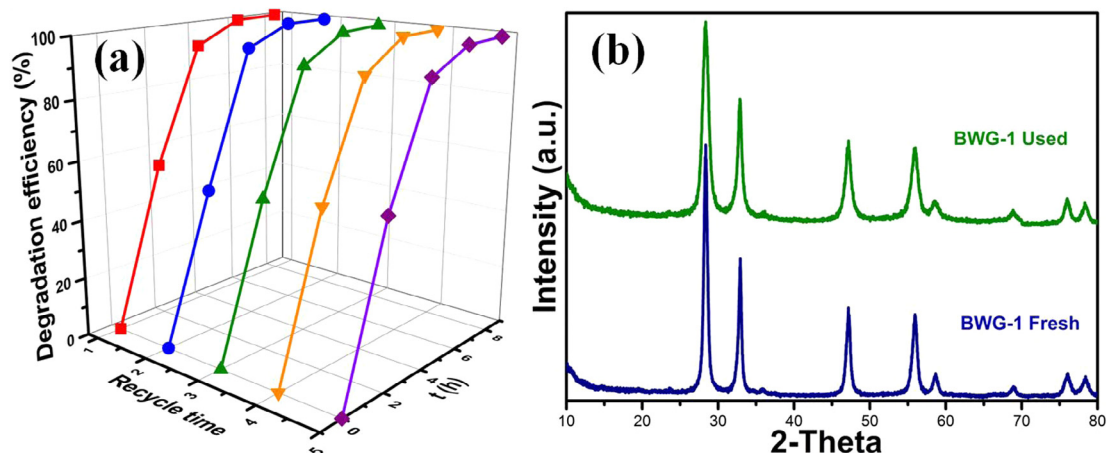


Fig. 12. (a) Cycling photocatalytic degradation of RhB using BWG-1 and (b) XRD patterns of BWG-1 acquired before and after the recycle experiment.

as-prepared and recycled samples, indicating that the BWG-1 composite possesses high photo-stability over prolonged irradiation time.

4. Conclusions

To sum up, we designed a simple and low-cost method for the controllable synthesis of $\text{Bi}_2\text{WO}_6/\text{RGO}$ hybrids under mild conditions, where the as-synthesized composites exhibited superior photocatalytic performances under sunlight irradiation as compared to that of pure Bi_2WO_6 . The 1 wt% $\text{Bi}_2\text{WO}_6/\text{RGO}$ hybrid with 1% wt RGO dosage had the optimal photocatalytic activity and different mineralization rate towards the degradation of RhB, MO, phenol, SMM and SN in aqueous solution. The improvement in the photocatalytic activity when incorporating RGO with Bi_2WO_6 hierarchical hollow microspheres might be owing to the enhanced light harvesting efficiency and improved charge separation efficiency of the composites. By investigating the time-resolved morphology and crystalline evolution of $\text{Bi}_2\text{WO}_6/\text{RGO}$, a possible mechanism for its formation process was proposed, which was ascribed to Ostwald ripening process based on Gibbs-Thomson law. Our work could provide new insights into rational design of sunlight responsive photocatalytic composites for meeting the growing demands for practical environmental applications.

Acknowledgements

The authors are grateful for the Basic Scientific and Technological Frontier Project of Henan Province (Grant No. 162300410046), the Innovation Scientists and Technicians Troop Construction Projects of Henan Province, China, the Research Start-up Foundation (Grant No. 5101219170107) and Youth Science Foundation (Grant No. 2015QK29) of Henan Normal University for the PhD, China. The authors would also like to thank the National Natural Science Foundation of China (Grants Nos. U1604137 and 21677047).

References

- Y. Lei, G. Zhao, Y. Zhang, M. Liu, L. Liu, B. Lv, J. Gao, Highly efficient and mild electrochemical incineration: mechanism and kinetic process of refractory aromatic hydrocarbon pollutants on superhydrophobic PbO_2 anode, *Environ. Sci. Technol.* 44 (2010) 7921–7927.
- X. Guan, Y. Sun, H. Qin, J. Li, I.M.C. Lo, D. He, H. Dong, The limitations of applying zero-valent iron technology in contaminants sequestration and the corresponding countermeasures: the development in zero-valent iron technology in the last two decades (1994–2014), *Water Res.* 75 (2015) 224–248.
- M.G. Alalm, S. Ookawara, D. Fukushi, A. Sato, A. Tawfik, Improved WO_3 photocatalytic efficiency using ZrO_2 and Ru for the degradation of carbofuran and ampicillin, *J. Hazard. Mater.* 302 (2016) 225–231.
- J. Xu, Z. Hao, C. Guo, Y. Zhang, Y. He, W. Meng, Photodegradation of sulfapyridine under simulated sunlight irradiation: kinetics, mechanism and toxicity evolution, *Chemosphere* 99 (2014) 186–191.
- H.F. Lai, C.C. Chen, Y.K. Chang, C.S. Lu, R.J. Wu, Efficient photocatalytic degradation of thiobencarb over BiVO_4 driven by visible light: parameter and reaction pathway investigations, *Sep. Purif. Technol.* 122 (2014) 78–86.
- Y.H.B. Liao, J.X. Wang, J.S. Lin, W.H. Chung, W.Y. Lin, C.C. Chen, Synthesis, photocatalytic activities and degradation mechanism of Bi_2WO_6 toward crystal violet dye, *Catal. Today* 174 (2011) 148–159.
- N.D. Phu, L.H. Hoang, X.B. Chen, M.H. Kong, H.C. Wen, W.C. Chou, Study of photocatalytic activities of Bi_2WO_6 nanoparticles synthesized by fast microwave-assisted method, *J. Alloys Compd.* 647 (2015) 123–128.
- W.L.W. Lee, S.T. Huang, J.L. Chang, J.Y. Chen, M.C. Cheng, C.C. Chen, Photodegradation of CV over nanocrystalline bismuth tungstate prepared by hydrothermal synthesis, *J. Mol. Catal. A* 361 (2012) 80–90.
- N. Tian, Y. Zhang, H. Huang, Y. He, Y. Guo, Influences of Gd substitution on the crystal structure and visible-light-driven photocatalytic performance of Bi_2WO_6 , *J. Phys. Chem. C* 118 (2014) 15640–15648.
- Y.H. Xiang, P. Ju, Y. Wang, Y. Sun, D. Zhang, J.Q. Yu, Chemical etching preparation of the $\text{Bi}_2\text{WO}_6/\text{BiOI}$ p-n heterojunction with enhanced photocatalytic antifouling activity under visible light irradiation, *Chem. Eng. J.* 288 (2016) 264–275.
- J. Tian, Y. Sang, G. Yu, H. Jiang, X. Mu, H. Liu, A Bi_2WO_6 -based hybrid photocatalyst with broad spectrum photocatalytic properties under UV, visible, and near-infrared irradiation, *Adv. Mater.* 25 (2013) 5075–5080.
- G. Tan, J. Huang, L. Zhang, H. Ren, A. Xia, An enhanced visible-light-driven photocatalyst: conduction band control of Bi_2WO_6 crystallites by Cu ion modification, *Ceram. Int.* 40 (2014) 11671–11679.
- Q.S. Wu, Y. Cui, L.M. Yang, G.Y. Zhang, D.Z. Gao, Facile in-situ photocatalysis of $\text{Ag}/\text{Bi}_2\text{WO}_6$ heterostructure with obviously enhanced performance, *Sep. Purif. Technol.* 142 (2015) 168–175.
- Y. Wang, X. Bai, C. Pan, J. He, Y. Zhu, Enhancement of photocatalytic activity of Bi_2WO_6 hybridized with graphite-like C_3N_4 , *J. Mater. Chem.* 22 (2012) 11568–11573.
- Y. Lei, C. Fang, J. Xu, Y. He, Enhanced photoelectric properties of $\text{CdSe}/\text{graphene}$ composites with various contents of graphene, *Ceram. Int.* 42 (2016) 5326–5330.
- M.Q. Yang, B. Weng, Y.J. Xu, Improving the visible light photoactivity of In_2S_3 -graphene nanocomposite via a simple surface charge modification approach, *Langmuir* 29 (2013) 10549–10558.
- X.Y. Li, L.H. Ai, J. Jiang, Nanoscale zerovalent iron decorated on graphene nanosheets for Cr(VI) removal from aqueous solution: surface corrosion retard induced the enhanced performance, *Chem. Eng. J.* 288 (2016) 789–797.
- J. Sun, Y. Chen, M.K. Priyadarshi, Z. Chen, A. Bachmatiuk, Z. Zou, Z. Chen, X. Song, Y. Gao, M.H. Rummeli, Y. Zhang, Z. Liu, Direct chemical vapor deposition-derived graphene glasses targeting wide ranged applications, *Nano Lett.* 15 (2015) 5846–5854.
- Y. Zhang, Y. Zhu, J. Yu, D. Yang, T.W. Ng, P.K. Wong, J.C. Yu, Enhanced photocatalytic water disinfection properties of Bi_2MoO_6 -RGO nanocomposites under visible light irradiation, *Nanoscale* 5 (2013) 6307–6310.
- W. Han, C. Zang, Z. Huang, H. Zhang, L. Ren, X. Qi, J. Zhong, Enhanced photocatalytic activities of three-dimensional graphene-based aerogel embedding TiO_2 nanoparticles and loading MoS_2 nanosheets as Co-catalyst, *Int. J. Hydrogen Energy* 39 (2014) 19502–19512.
- S.Y. Chou, W.H. Chung, L.W. Chen, Y.M. Dai, W.Y. Lin, J.H. Lin, C.C. Chen, A series of BiO_x/GO photocatalysts: synthesis, characterization, activity, and mechanism, *RSC Adv.* 6 (2016) 82743–82758.
- S.Y. Chou, C.C. Chen, Y.M. Dai, J.H. Lin, W.W. Lee, Novel synthesis of bismuth oxyiodide/graphitic carbon nitride nanocomposites with enhanced visible-light photocatalytic activity, *RSC Adv.* 6 (2016) 33478–33491.
- X. Bai, L. Wang, R. Zong, Y. Lv, Y. Sun, Y. Zhu, Performance enhancement of ZnO photocatalyst via synergic effect of surface oxygen defect and graphene hybridization, *Langmuir* 29 (2013) 3097–3105.
- E. Gao, W. Wang, M. Shang, J. Xu, Synthesis and enhanced photocatalytic performance of graphene- Bi_2WO_6 composite, *Phys. Chem. Chem. Phys.* 13 (2011) 2887–2893.
- H. Ma, J. Shen, M. Shi, X. Lu, Z. Li, Y. Long, N. Li, M. Ye, Significant enhanced performance for Rhodamine B, phenol and Cr(VI) removal by Bi_2WO_6 nanocomposites via reduced graphene oxide modification, *Appl. Catal. B* 121–122 (2012) 198–205.
- S. Dong, J. Feng, Y. Li, L. Hu, M. Liu, Y. Wang, Y. Pi, J. Sun, J. Sun, Shape-controlled synthesis of BiVO_4 hierarchical structures with unique natural-sunlight-driven photocatalytic activity, *Appl. Catal. B* 152 (2014) 413–424.
- M. Shang, W. Wang, H. Xu, New Bi_2WO_6 nanocages with high visible-light-driven photocatalytic activities prepared in refluxing EG, *Cryst. Growth Des.* 9 (2009) 991–996.
- S. Dong, J. Sun, Y. Li, C. Yu, Y. Li, J. Sun, ZnSnO_3 hollow nanospheres/reduced graphene oxide nanocomposites as high-performance photocatalysts for degradation of metronidazole, *Appl. Catal. B* 144 (2014) 386–393.
- S. Dong, L. Hu, J. Feng, Y. Pi, Q. Li, Y. Li, M. Liu, J. Sun, J. Sun, Ultrasonic-assisted rational design of uniform rhombus-shaped ZnMoO_4 on graphene for advanced sunlight-driven photocatalysts, functional supercapacitor electrodes, and antibacterial platforms, *RSC Adv.* 4 (2014) 64994–65003.
- S. Dong, Y. Cui, Y. Wang, Y. Li, L. Hu, J. Sun, J. Sun, Designing three-dimensional acicular sheaf shaped BiVO_4 /reduced graphene oxide composites for efficient sunlight-driven photocatalytic degradation of dye wastewater, *Chem. Eng. J.* 249 (2014) 102–110.
- J. Yu, J. Xiong, B. Cheng, Y. Yu, J. Wang, Hydrothermal preparation and visible-light photocatalytic activity of Bi_2WO_6 powders, *J. Solid State Chem.* 178 (2005) 1968–1972.
- P. Tang, H. Chen, F. Cao, One-step preparation of bismuth tungstate nanodisks with visible-light photocatalytic activity, *Mater. Lett.* 68 (2012) 171–173.
- H. Li, W. Hou, X. Tao, N. Du, Conjugated polyene-modified Bi_2MO_6 ($M = \text{Mo}$ or W) for enhancing visible light photocatalytic activity, *Appl. Catal. B* 172–173 (2015) 27–36.
- J. Yang, X. Wang, X. Zhao, J. Dai, S. Mo, Synthesis of uniform Bi_2WO_6 -reduced graphene oxide nanocomposites with significantly enhanced photocatalytic reduction activity, *J. Phys. Chem. C* 119 (2015) 3068–3078.
- H.Q. Li, Y.M. Cui, W.S. Hong, B.L. Xu, Enhanced photocatalytic activities of $\text{BiOI}/\text{ZnSn}(\text{OH})_6$ composites towards the degradation of phenol and photocatalytic H_2 production, *Chem. Eng. J.* 228 (2013) 1110–1120.
- D. Wang, L. Guo, Y. Zhen, L. Yue, G. Xue, F. Fu, AgBr quantum dots decorated mesoporous Bi_2WO_6 architectures with enhanced photocatalytic activities for methylene blue, *J. Mater. Chem. A* 2 (2014) 11716–11727.
- H.P. Lin, W.W. Lee, S.T. Huang, L.W. Chen, T.W. Yeh, J.Y. Fu, C.C. Chen, Controlled hydrothermal synthesis of $\text{PbBiO}_3/\text{BiOBr}$ heterojunction with enhanced visible-light-driven photocatalytic activities, *J. Mol. Catal. A* 417 (2016) 168–183.

- [38] H.P. Lin, C.C. Chen, W.W. Lee, Y.Y. Lai, J.Y. Chen, Y.Q. Chen, J.Y. Fu, Synthesis of a $\text{SrFeO}_{3-x}/\text{g-C}_3\text{N}_4$ heterojunction with improved visible-light photocatalytic activities in chloramphenicol and crystal violet degradation, *RSC Adv.* 6 (2016) 2323–2336.
- [39] C.T. Yang, W.W. Lee, H.P. Lin, Y.M. Dai, H.T. Chi, C.C. Chen, A novel heterojunction photocatalyst, $\text{Bi}_2\text{SiO}_5/\text{g-C}_3\text{N}_4$: synthesis, characterization, photocatalytic activity, and mechanism, *RSC Adv.* 6 (2016) 40664–40675.
- [40] W.W. Lee, C.S. Lu, C.W. Chuang, Y.J. Chen, J.Y. Fu, C.W. Siao, C.C. Chen, Synthesis of bismuth oxyiodides and their composites: characterization, photocatalytic activity, and degradation mechanisms, *RSC Adv.* 5 (2015) 23450–23463.
- [41] Y.R. Jiang, H.P. Lin, W.H. Chung, Y.M. Dai, W.Y. Lin, C.C. Chen, Controlled hydrothermal synthesis of $\text{BiO}_x\text{Cl}_y/\text{BiO}_m\text{I}_n$ composites exhibiting visible-light photocatalytic degradation of crystal violet, *J. Hazard. Mater.* 283 (2015) 787–805.
- [42] Y.R. Jiang, S.Y. Chou, J.L. Chang, S.T. Huang, H.P. Lin, C.C. Chen, Hydrothermal synthesis of bismuth oxybromide-bismuth oxyiodide composites with high visible light photocatalytic performance for the degradation of CV and phenol, *RSC Adv.* 5 (2015) 30851–30860.
- [43] S.T. Huang, Y.R. Jiang, S.Y. Chou, Y.M. Dai, C.C. Chen, Synthesis, characterization, photocatalytic activity of visible-light-responsive photocatalysts $\text{BiO}_x\text{Cl}_y/\text{BiO}_m\text{Br}_n$ by controlled hydrothermal method, *J. Mol. Catal. A* 391 (2014) 105–120.